

Swift heavy ion track formation in SiC films under high-temperature irradiation

D.I. Zainutdinov^{a*}, A.E. Volkov^a

^a*P.N. Lebedev Physical Institute of the Russian Academy of Sciences, Leninskij pr., 53, 119991 Moscow, Russia*

Abstract

The resistance of bulk silicon carbide (SiC) to impacts of swift heavy ions (SHI) decelerating at room temperature in the electronic stopping regime is well known. However, the effect of the SiC film thickness on the formation and structure of SHI tracks over a wide range of irradiation temperatures remains unexplored. To address this disadvantage, we utilize a model sensitive to irradiation temperature that describes all stages of ion track formation: from material excitation, considering the emission of excited electrons from the film surface (MC code TREKIS-3), to the reaction of the material's atomic system to the excitation (classical molecular dynamics). We observed the formation of two different types of nanostructures on the surface of SiC films with thicknesses ranging from 10 nm to 100 nm when irradiated with 710 MeV Bi ions: craters and hills. The type of nanostructure formed depended on the irradiation temperature. The transition irradiation temperature (T_{tr}) from hills to craters grows with the film thickness and follows an empirical relation $T_{tr} = T_{tr}^{cr} \left(1 - \left(1 + \left(\frac{L}{L_{cr}} \right)^2 \right)^{-\frac{1}{2}} \right)$ with $T_{tr}^{cr} = 1534$ K and $L_{cr} = 2.8$ nm. That means such a transition should occur in bulk SiC at the irradiation temperature of ≈ 1534 K.

Keywords: ion-solid interactions; modeling; multiscale; ceramic; electron emission, Surface and Films, hillocks, craters

1. Introduction

Silicon carbide (SiC) is widely used in modern solid-state microelectronics and nuclear technologies due to its unique physical and chemical characteristics. Nowadays, there is a trend towards miniaturization of devices based on SiC [1], as well as their application in extreme conditions, which include both high temperatures and ionizing radiation [2,3]. In particular, it is of interest to study the response of SiC to irradiation by swift heavy ions (SHI) with masses larger than $10m_p$ (m_p is the mass of a proton) and energies of 1-10 MeV/nucleon providing the ion stopping in matter in the electronic energy loss regime. Impacts of these ions can cause the failure of space SiC electronics due to the so-called single-event burnout phenomenon [4,5], or lead to the degradation of structural components in fission and fusion reactors [6].

*Corresponding author: d.zainutdinov@lebedev.ru

Although some progress has been made in studying the effect of SHIs at high irradiation temperatures on bulk SiC crystals [7–10], the question of the influence of the size of these crystals on their response to irradiation with SHI beams remains open. Changes in crystal size can increase the role of the surface in the kinetics of defect formation as well as in the evolution of defects in the irradiated material [11–13] thereby significantly altering the response of the target to ion irradiation. Also, the SHI - induced damage near the SiC surface and how this damage changes with the irradiation temperature have not yet been investigated.

To study the mechanisms that provide structural changes in SiC films irradiated with SHIs at high temperatures, we performed simulations within the well-proven multiscale model. The approach combines the Monte Carlo (MC) code TREKIS-3 [14,15], which describes the short-term excitation of the electron and ion systems of a target (within ~ 100 fs) taking into account the emission of excited electrons from the surface [16], and the molecular dynamics (MD) code LAMMPS [17] for modelling the subsequent response of the atomic lattice to the excitation. Based on the simulation data, we constructed a formula that allows for a qualitative estimate of the shape of tracks depending on the thickness of a SiC film and the irradiation temperature. In our work, we considered hexagonal 6H-SiC films because they are stable at high temperatures [18].

2. Model

The modeling of the SHI track formation in SiC films consists of two stages. In the first stage, the TREKIS-3 MC code is used to simulate the passage of SHI through the film, the excitation and relaxation of the target's electron system, taking into account its interaction with the target's atoms, as well as the emission of excited electrons from the film surface. The profile of energy transferred to the lattice by the relaxation of electronic excitation, approximately at 100 fs after the ion impact, obtained at this stage is converted into the initial velocities of atoms for the subsequent prediction of structural changes in the lattice using classical molecular dynamics (LAMMPS code).

2.1. Monte-Carlo simulation

The MC code TREKIS-3 describes the ionization of the target along the SHI trajectory, transport of valence holes and excited electrons including the emission of electrons from the film surface. TREKIS-3 models the scattering of electrons on the atomic lattice transferring kinetic energy to atoms as well as on target electrons resulting in the ionization of matter with the formation of secondary holes and electrons. This code also describes the Auger decay of holes accompanied by electron emission, radiative decay with photon emission, and further photon transport and absorption [14,15]. The code does not take into account interactions of an SHI with

target atoms due to the negligible cross sections of this process in the range of ion energies considered in this paper.

The radial distribution of the energy density transferred to atoms in the vicinity of the ion trajectory forms the main result of the MC modeling. The atomic lattice accumulates the additional energy through two channels: (a) scattering of excited electrons and valence holes as well as (b) nonthermal heating [19] resulting from an acceleration of atoms caused by a sharp change in the interatomic potential due to fast extreme excitation of the electron system of a target. Following the Ref. [20], nonthermal atomic heating can be taken into account by converting the potential energy of electron-hole pairs into the kinetic energy of atoms at the moment of cooling down of the electron system (approximately 100 fs after the ion impact) due to the effect of band gap collapse.

TREKIS-3 is based on the asymptotic trajectory method of event-by-event simulation, in which the scattering of a particle is described by cross sections that take into account the collective response of the target electrons and atoms to excitation in the linear response (first order Born) approximation [21].

In this approximation, the non-ionizing scattering cross section of electrons and holes on the atomic system is expressed through the atomic dynamical structure factor (DSF) $S_{at}(\omega, q, T_{irr})$ and describes the energy exchange with the atomic ensemble taking into account, if necessary, its collective response to the excitation:

$$\frac{d^2\sigma_{at}}{d(\hbar q)d(\hbar\omega)} = \frac{qm_{e,h}}{4\pi\hbar^4 E} |U_{p-at}(q)|^2 S_{at}(\omega, q, T_{irr}). \quad (1)$$

Here $\hbar\omega$ and $\hbar q$ are the energy and momentum transferred from the projectile to target atoms, and \hbar is Planck's constant. E is the projectile energy, m_e is the electron mass, m_h is the mass of a valence hole obtained in the one-band model [15] from the density of valence band states [22]. $U_{p-at}(q) = 4\pi e^2/(q^2 + (l_{scr})^{-2})$ the interaction potential between the projectile (electron or valence hole) and a screened lattice ion, with the screening parameter $l_{scr}=0.14$ nm from Ref. [9], where e is the electron charge.

A change in the irradiation temperature leads to a change in the number of phonons in the crystal modes, the phonon lifetime, and their spectrum due to the expansion of the crystal lattice upon heating [23,24]. This leads to a change in the atomic DSF and hence the scattering cross sections (1) on the atomic system. To account for the temperature dependence of the DSF, we recalculated the cross sections separately for each temperature using the algorithm described in Ref. [9]. In this

approach, the classical atomic DSF ($S_{at}^{cl}(\omega, q, T_{irr})$), which is symmetric on transferred energy $\hbar\omega$, is calculated from the trajectories of target atoms obtained from the classical MD simulation at a fixed temperature. On the other hand, the quantum DSF $S_{at}(\omega, q, T_{irr})$ is asymmetric on the transferred energy: $S_{at}(\omega, q, T_{irr}) = \exp(\hbar\omega/T_{irr}) \cdot S_{at}(-\omega, q, T_{irr})$ and can be recovered from the classical DSF through the multiplication by the ‘Harmonic’ quantum correction factor [25–27]:

$$S_{at}(\omega, q, T_{irr}) = \frac{\hbar\omega/k_b T_{irr}}{1 - \exp(-\hbar\omega/k_b T_{irr})} S_{at}^{cl}(\omega, q, T_{irr}) \quad (2)$$

The obtained quantum atomic DSF satisfies the quantum sum rule [9] and contains temperature in two parts: in the quantum correction factor and in the classical DSF, where the temperature is present in the trajectories of atoms in the form of their velocity distribution.

The particle scattering cross section (SHI, electrons, valence holes) on the electron subsystem is conveniently expressed through the imaginary part of the inverse complex dielectric function (CDF) of the electrons [28] – the loss function (LF), which weakly changes with the irradiation temperature:

$$\frac{d^2\sigma_e}{d(\hbar q)d(\hbar\omega)} = \frac{[Z_{eff}^2(v)e]^2}{\hbar^2\pi E n_e} \frac{m_{e,h}}{\hbar q} \left(1 - e^{-\frac{\hbar\omega}{k_b T_{irr}}}\right)^{-1} \text{Im}\left[-\frac{1}{\varepsilon_e(\omega, q)}\right], \quad (3)$$

Here n_e is the concentration of electrons in the medium, and $\text{Im}[-\varepsilon_e^{-1}(\omega, q)]$ is the electron part of the LF, which is presented for SiC in Ref. [9]. The scattering cross section on the electronic subsystem accounts for ionization of the atomic shells and valence band. The effective charge of an SHI, $Z_{eff}(v)$, is estimated using the Barkas formula [19,29]:

$$Z_{eff}(v_{ion}) = Z_{ion} \left[1 - \exp\left(-\frac{v_{ion}}{v_0} Z_{ion}^{-\frac{2}{3}}\right)\right], \quad (4)$$

where Z_{ion} is the nuclear charge of the incident ion, $v_0 = c/125$, where c is the speed of light in vacuum. The effective charges of electrons and valence holes are equal to unit.

The transition probability of electrons from the film surface to vacuum in TREKIS-3 [16] is determined by Eq. (5), which takes into account their reflection and the effect of quantum tunneling through the surface barrier:

$$\tau(E) = \frac{1}{1 + \exp(\gamma(E_1 - E))} \quad (5)$$

Here E is the electron energy, E_1 is a parameter that depends on the height of the emission barrier, and γ is a parameter that depends on the characteristic spatial scale of the barrier [30]. The energy of the emitted electron is counted from the vacuum energy level (kinetic energy of the electron minus the work function). The parameters E_1 and γ depend on the substance. The procedure for determining them for SiC as well as the corresponding Eckart-type barrier are described in the next section.

2.2. Transmission coefficient and emission barrier in SiC

For the transition from a sample to a vacuum, an electron must overcome a potential barrier. Eckart has proposed the form of this barrier $V(z)$, which allows for the exact calculation of the transmission coefficient [31]:

$$V(z) = - \left[\frac{W\xi}{1-\xi} + \frac{B\xi}{(1-\xi)^2} \right] \quad (6)$$

here $\xi = -\exp(2\pi z/L)$, z is a Cartesian coordinate. Negative values of z determine the potential inside the target, where $V(z \ll -L) \approx 0$, and positive values on the surface $V(z \gg L) \approx W$ with W being the work function. L is the characteristic length of the barrier (width of the transition region is $2L$) and W_1 is its height determined by the work function and the parameter B :

$$W_1 = \frac{(W+B)^2}{4B} \quad (7)$$

The simple formula (5) can be used for the transmission coefficient $\tau(E)$ for a narrow Eckart-type barrier, when $W_1 > W$ [30]. Following this work, we determined the parameters E_1 and γ by fitting the experimental spectrum of emitted electrons [32] with the function:

$$\tilde{J}(E) = \frac{(E+W)^{\frac{1}{2}} \left[C_1 \exp\left(-\frac{E}{\epsilon}\right) + C_2 \exp\left(-\frac{E}{2\epsilon}\right) \right]}{1 + \exp(\gamma(E_1 - E - W))} \quad (8)$$

where $\tilde{J}(E)$ is the number of electrons emitted into the vacuum from a unit of surface, per unit time, per unit energy; ϵ is the mean energy exchange between the secondary electrons and the medium at the free path length; C_1 and C_2 are related to the intensity of the ϵ and 2ϵ contributions to the distribution, respectively.

Table 1 shows the values of the parameters in Eq. (8) that provide good agreement with the experimental data on thermionic emission (see Fig. 1a) [32] from the (001) surface of 6H-SiC crystal. The value of the work function $W = 4.5$ eV was taken from Ref. [33].

Table 1 Values of parameters of function (8) , corresponding to the best agreement with the experimental data [32] on thermionic emission of electrons from 6H-SiC .

W, eV	C_1	C_2	ϵ, eV	γ, eV^{-1}	E_1, eV
4.5	61.2	5.3	1.58	8.48	4.68

We obtained the parameters $L = 1.2$ nm and $B = 6.97$ eV of the Eckart-type barrier corresponding to the experimental values of E_1 , γ , W from Table 1 using the system of equations (7-8) from Ref. [30].

Fig. 1b shows the transmission coefficient through the barrier which corresponds to the parameters E_1 and γ from Table 1 and takes into account the reflection of electrons with energies $E < W$.

Fig. 1c illustrates the dependence of the Eckart-type barrier in SiC on the distance z to the surface. It can be seen that our assumption $W_1 > W$ is valid for the barrier in SiC, the difference between the barrier height $W_1 = 4.72$ eV and the work function $W = 4.5$ eV occurs due to the existence of an image potential in SiC. Following Ref.[33], we ignore shape changes of the barrier with target temperature increase.

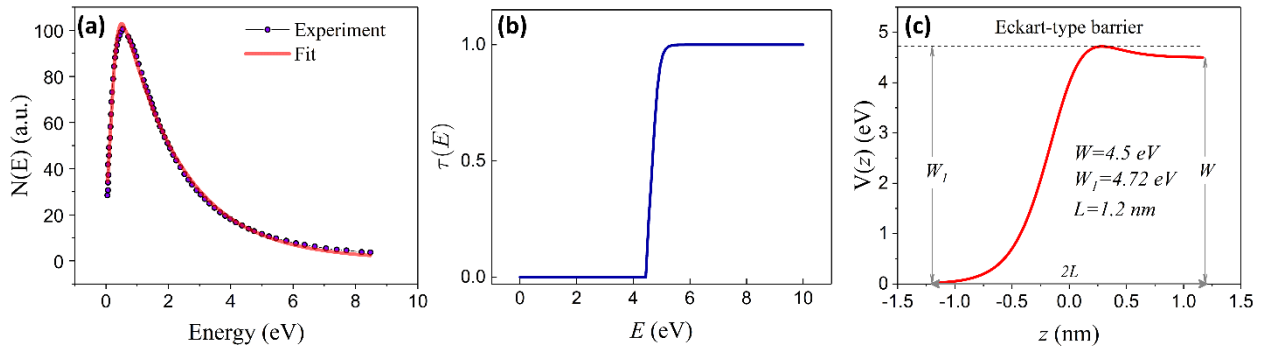


Fig. 1 (a) Experimental distribution of thermal-emitted electrons from the SiC surface [32] and its fitting with Eq. (8); (b) Transmission coefficient (5) through the surface potential barrier in SiC; (c) Shape of the Eckart-type barrier (6) in SiC

2.3. Molecular-dynamics model

We prepared rectangular parallelepiped-shaped films with thicknesses ranging from 10 nm to 100 nm containing 6H-SiC crystals with crystal axes $[10\bar{1}0]$, $[\bar{1}2\bar{1}0]$, and $[0001]$. In the simulation cell, free boundaries conditions were applied at a distance of 30 nm from the film surfaces in the direction along the SHI trajectory $[0001]$. Periodic boundary conditions were used in the $[10\bar{1}0]$ and $[\bar{1}2\bar{1}0]$ directions. The dimensions of the films in the (001) plane are $28 \times 29 \text{ nm}^2$.

Prior to simulations, we minimized the energy in the films with Vashishta's potential [34] and performed a two-step equilibration procedure at a fixed temperature, as described in Ref. [35].

The kinetic energy for each atom in the track was determined randomly according to a Gaussian distribution of the atomic velocities. To build up this distribution, we used the average energy density released in the atomic lattice at the atomic position by the time of electron cooling, taken from the TREKIS simulation at $\sim 100 \text{ fs}$ after the ion impact [36,37].

We modeled the evolution of the atomic structure after the SHI passage in the LAMMPS code using Vashishta's interatomic potential [34] and the Verlet algorithm in a simulation cell that includes a film with open surfaces. We used a variable time step corresponding to a maximum atomic displacement of 0.1 \AA . The modeling finished when the track core cooled to the irradiation temperature ($\sim 200\text{-}300 \text{ ps}$). During the simulation, the Berendsen thermostat [38] with a damping time of 20 fs was applied in a 5 \AA thick layer at the cell boundaries around the ion trajectory.

3. Results and Discussion

3.1. Excitation of SiC film with electron emission

Ref. [39] demonstrated that the effect of electron emission on ion track formation is most significant in thin films up to 15 nm thick. Therefore, to investigate the influence of irradiation temperature on the excitation of the electron system of a target taking into account electron emission, we performed a series of MC simulations of irradiation of a 10 nm thick SiC film with Bi 710 MeV ion ($dE/dx \approx 35 \text{ keV/nm}$) at different temperatures.

For the transition of excited electrons from the film surface to vacuum, two conditions must be satisfied:

1. The electron velocity component normal to the film surface directed towards the vacuum must be nonzero [30];

2. The electron energy must be greater than the work function (see Fig. 1b).

It means that the number of emitted electrons and, consequently, the profile of the energy deposited in the atomic lattice at different irradiation temperatures are determined by, at least, two processes: the isotropization of excited electron momentum and their deceleration in the material.

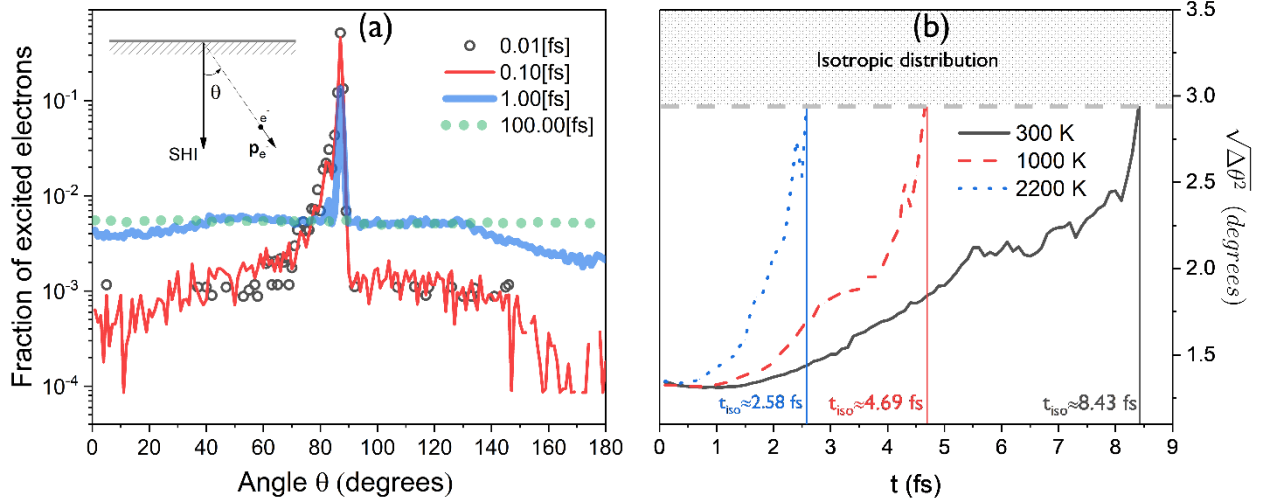


Fig. 2 (a) Distribution of the momenta of excited electrons along the zenith angle θ after irradiation of a 10 nm thick SiC film with Bi 710 MeV ion at 300 K, (b) Temporal evolution of the width at half maximum at $\theta=90^\circ$, in the distribution of excited electrons along the zenith angle θ in 10 nm thick SiC film irradiated with Bi 710 MeV ion at different temperatures.

The passage of an SHI through the film perpendicular to its surface leads to the formation of a δ -electron front after ~ 0.01 fs, propagating predominantly perpendicular to the ion trajectory and parallel to the surface. Consequently, the angular distribution of excited electrons relative to the zenith angle θ (see Fig. 2a) at the moment of 0.01 fs exhibits a pronounced peak centered at about $\theta \approx 90^\circ$, where $\theta = 0^\circ$ corresponds to the electron motion along the ion direction, and $\theta = 180^\circ$ - in the opposite direction. The small variation in the momentum direction of these electrons leads to the possibility that a small fraction of these electrons may escape the film within 0.1 fs after irradiation, as can be seen in Fig. 3a. The fraction of escaped electrons at these times slowly increases with the irradiation temperature due to the increase in the number of excited electrons in the track, as shown in Ref. [9]. However, this trend is very weak and has little effect on the final profile of electrons escaped over 100 fs at different temperatures.

Starting at 0.1 fs, the scattering of electrons on the atomic lattice leads to isotropization of their zenith angle distribution. Fig. 2a shows how the sharp peak at 90° at 0.1 fs in the distribution of excited electrons formed at room irradiation temperature broadens and decreases in height, passing

to a uniform distribution by 100 fs. As a result, some electrons leave the film during the isotropization process.

Moreover, increasing the irradiation temperature leads to an increase in the isotropization rate, as shown in Fig. 2b. For example, at $T_{irr} = 300$ K electrons are isotropized during the time $t \approx 8.4$ fs, at $T_{irr} = 1000$ K during $t \approx 4.7$ fs, and at $T_{irr} = 2200$ K during $t \approx 2.6$ fs. Here we used the width of the peak at half-height in the electron zenith angle θ distribution, denoted by $\sqrt{\Delta\theta^2}$, as a measure of the distribution's isotropy in Fig. 2b.

The polynomial fit of the data in Fig. 3a shows an increase in the number of emitted electrons from the SiC film 100 fs after irradiation at temperatures ranging from 300 K to 500 K. This increase can be associated with a rise in the isotropization rate of excited electrons, whereby electrons with above-barrier energy reach the surface before losing their energy due to lattice scattering.

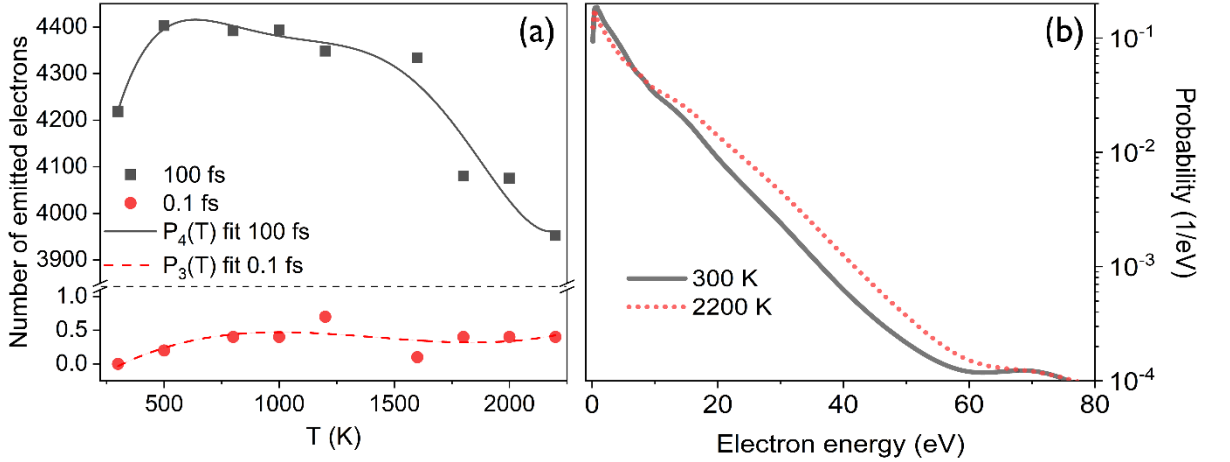


Fig. 3 (a) Total number of emitted electrons from a 10 nm thick SiC film at 0.1 fs and 100 fs after Bi 710 MeV ion irradiation at different temperatures averaged from 10 MC simulations and their approximations by third- and fourth-degree polynomials, respectively; (b) Normalized kinetic energy spectra of secondary electrons emitted from a 10 nm thick SiC film after Bi 710 MeV ion impact at 300 K and 2200 K

However, starting from $T_{irr} = 500$ K, as shown in Fig. 3a, increasing the irradiation temperature leads to a decrease in the number of emitted electrons. This decrease can be associated with an increase in the energy loss of excited electrons per unit path caused by their scattering on phonons (see Ref. [9]). A similar trend was observed experimentally [40] in the range of 463-659 K when the bulk SiC target was irradiated with Xe^{17+} ions with energies of 3.2 MeV and 4 MeV. Apparently, this trend at high irradiation temperatures is not associated with a change in the work

function, which practically does not change with temperature [33], but is determined by the scattering of excited electrons on the atomic system [41].

To investigate the effect of electron emission on the profile of energy deposited in the atomic lattice in an SHI track, we performed a series of MC simulations of a 10 nm SiC thin film irradiated with a 710 MeV Bi ion at various temperatures: (i) including electron emission and (ii) with periodic boundary conditions (bulk simulations).

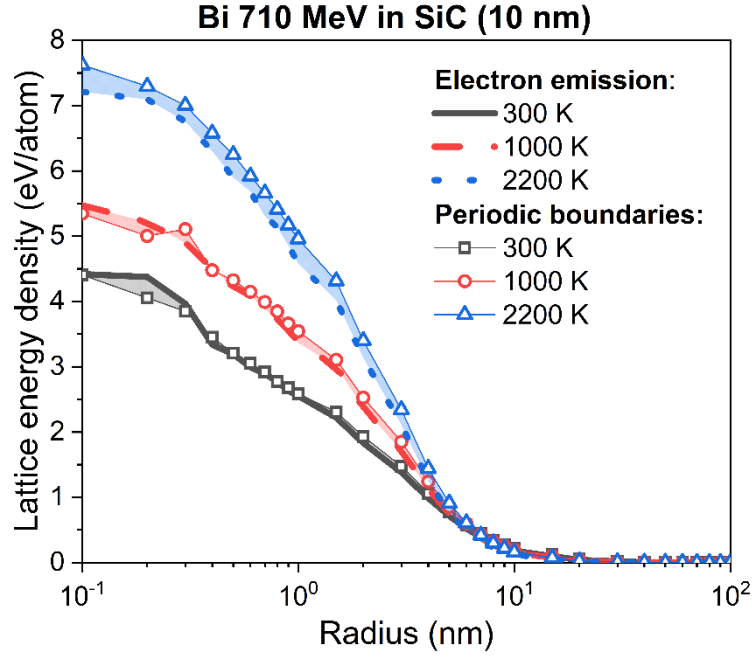


Fig. 4 Profiles of the additional lattice energy of 10 nm thick SiC film irradiated with a 710 MeV Bi ions at different temperatures. The color indicates the difference between the profiles obtained at the same temperature with and without electron emission .

Fig. 4 shows the radial distributions of the energy density transferred to the lattice in the tracks of 710 MeV Bi ions at different irradiation temperatures for these two cases. Evidently, the influence of emission on the deposited energy profile is noticeable only at high irradiation temperatures, in our case at $T_{irr} \approx 2200$ K. In the simulations with emission, less energy is transferred to the lattice than in the simulations with the periodic boundary conditions. However, Fig. 3a shows that at these high temperatures (for example $T_{irr} \approx 2200$ K) the number of emitted electrons is much smaller than their number at lower irradiation temperatures. As a result, increasing the irradiation temperature suppresses the process of electron emission, but at the same

time increases the role of electron emission in the formation of the final profile of the energy transferred to the atomic system.

Qualitatively, it can be associated with an increase in the fraction of phonon absorption in the scattering of electrons on the atomic lattice, which increases with irradiation temperature due to a decrease in the asymmetry of the atomic DSF in terms of transferred energy (see Eq. (2)). As a result, Fig. 5 shows that the rate of energy transfer to the lattice decreases with irradiation temperature. However, its temporal evolution remains unchanged: increasing the time up to about 20 fs is associated with the formation of “slow” electrons in cascades, which are predominantly scattered on the lattice, and a further decrease associated with the cooling of the electronic subsystem.

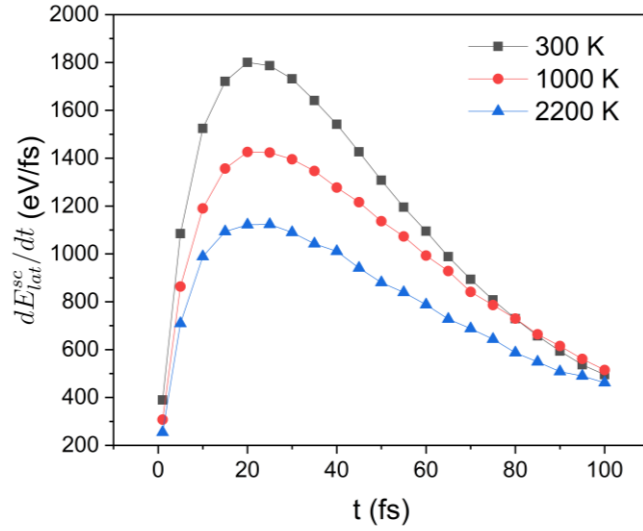


Fig. 5 The energy transfer rate to the entire atomic lattice of a 10 nm thick SiC film through the scattering of excited electrons in the track of 710 MeV Bi ions at different irradiation temperatures, taking into account electron emission.

Due to the decrease of the energy transfer rate, at high irradiation temperatures hot electrons escape the film before transferring all their energy to atoms. This leads to less heating of the film compared to the simulations with the periodic boundary conditions. Fig. 3b illustrates the normalized kinetic-energy distribution function of the emitted electrons, where the fraction of high-energy electrons increases with the irradiation temperature. However, the difference between the profiles of the energy deposited to atoms, obtained taking into account the emission and without it, is small ($\sim 8\%$, see Fig. 4) and, as shown in Ref. [39], becomes smaller with increasing

film thickness. Therefore, to better utilize computational resources for films thicker than 30 nm, we used profiles obtained in the simulations with periodic boundary conditions.

3.2. Structural changes in a 10 nm thick SiC film

Fig. 6a shows the temporal evolution of the atomic structure in a 10 nm thick SiC film after 710 MeV Bi ion impact at room temperature. It can be seen that during 5 ps, a molten cylindrical column with a diameter of $d \approx 7$ nm is formed in the track center. Thermal expansion of the molten region leads to “the squeezing” of some substance onto the film surface.

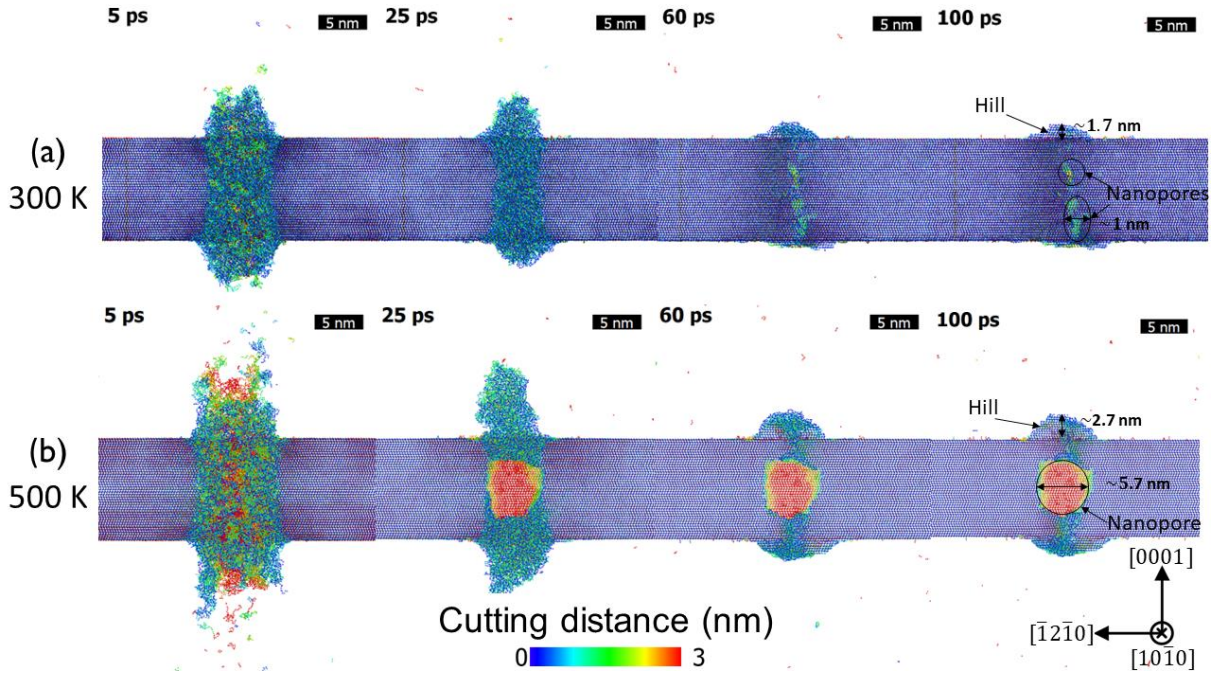


Fig. 6 Temporal evolution of the atomic structure of 10 nm thick SiC film after 710 MeV Bi ion impact (a) at 300 K and (b) at 500 K. The distance to the slice along the ion trajectory in the $(10\bar{1}0)$ plane is highlighted.

Over the next 95 ps, the molten region recrystallizes. Moreover, the recrystallization rate is faster in the layers farthest from the surfaces. For example, Fig. 6a illustrates that at time 25 ps, the molten region has an hourglass shape. Starting from 35 ps, dislocations are formed at the edges of the disordered region near the film surface (see Fig. 7a). By 60 ps after irradiation, the track inside the plate is almost completely restored, but the surface hillocks still have a disordered structure (see Fig. 6a). Then, over the next 40 ps, the hillocks also recrystallize, with the recrystallization front moving away from the film surface. As a result, hillocks remain on the film surfaces at 100 ps after irradiation. The fraction of the crystalline state in them is $\approx 12\%$. The highest hillock has $h \approx 1.7$ nm height and $d \approx 6$ nm diameter. Nanocavities with a diameter of

$d \approx 1$ nm surrounded by dislocations (see Fig. 7a) remain in the film volume along the ion trajectory. The surface of the nanocavities has a disordered structure consisting of point defects and defect clusters.

The irradiation of the same film with 710 MeV Bi ion at 500 K initiates similar stages of track formation (see Fig. 6b). However, dislocations form later: starting from 60 ps (see Fig. 7b). The main effect of the irradiation at 500 K manifests in the sizes of the residual defects: the height of the largest hillock is $h \approx 2.7$ nm, its diameter is $d \approx 7.6$ nm and the diameter of the inside cavity is $d \approx 5.7$ nm. The higher irradiation temperature also changes the defect composition: the crystallinity of the hillock increases to 31.4% , the surface of the cavity also becomes crystalline. The dislocations at the edges of the cavity remain only near the film surface (see Fig. 7b).

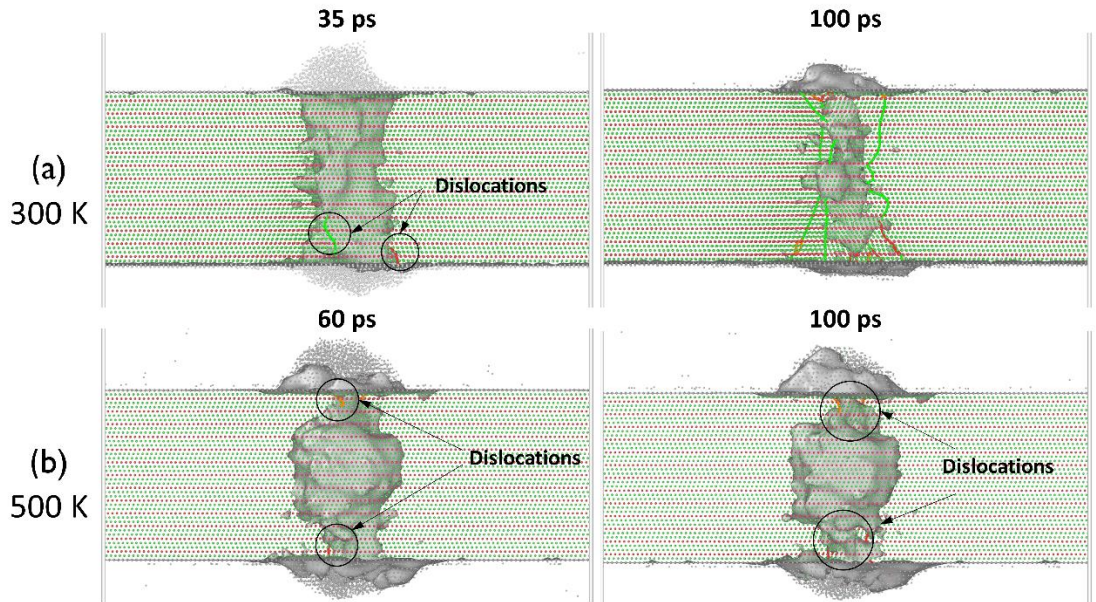


Fig. 7 Carbon sublattice of a 10 nm thick SiC film with highlighted dislocation lines and disordered region at different times after impacts of 710 MeV Bi ions (a) at 300 K and (b) at 500 K.

Note that the dislocations in Fig. 7, which we observed in the track at different irradiation temperatures, do not move away. As a result, they do not participate in the process of nanocavity formation by the mass transfer from the track core, as was observed in the bulk simulations [9]. Therefore, the mechanism of formation of nanocavities inside the film near the surface is associated with the displacement of a part of the substance to the film surface or ejection of substance droplets, as will be shown further at higher irradiation temperatures.

Fig. 8a shows a 10 nm thick SiC film after atomic structure relaxation (200 ps after an ion impact) in a slice along the trajectory of 710 MeV Bi ion at different irradiation temperatures.

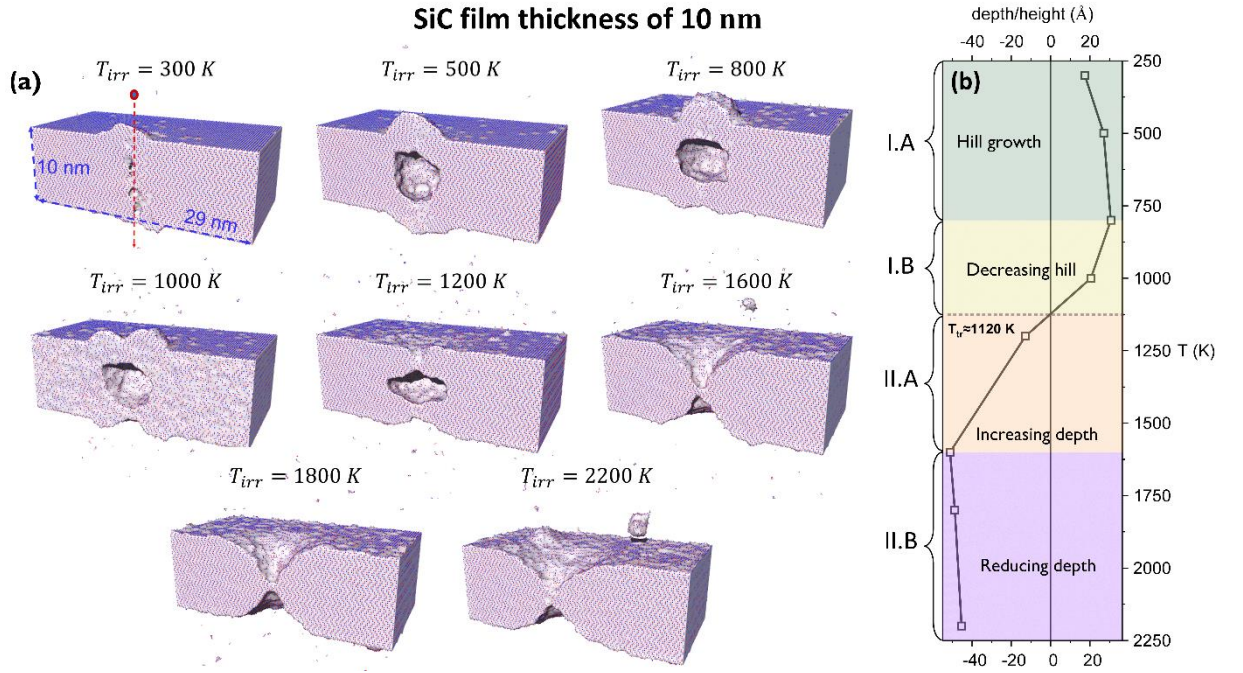


Fig. 8 (a) 10 nm thick SiC film 200 ps after impacts of 710 MeV Bi ion at different temperatures, (b) hillock height/crater depth as a function of irradiation temperature

The presented results show that the temperature scale can be divided into four regions, which are illustrated in Fig. 8b:

- I.A** Hillocks form on the film surfaces at irradiation temperatures up to 800 K. Their height increases with the irradiation temperature. At the same time, nanocavities remain in the film volume along the ion trajectory. Their volumes also increase with the irradiation temperature.
- I.B** An increase in the irradiation temperature in the range from 800 K to 1120 K leads to a decrease in the height of the hillocks, while the cavity sizes do not change;
- II.A** At the irradiation temperature ranging from 1120 K to 1600 K, the track geometry changes: a hillock transforms into a crater. The temperature increase lead to a decrease in the size of the cavity inside the film and an increase in the crater depth;
- II.B** At the irradiation temperatures above 1600 K, craters connected by a thin bridge remain on the film surfaces (see Fig. 8a). In this case, the track does not contain cavities. An increase in the irradiation temperature leads to a thickening of the bridge and, consequently, a reduction in the crater depth. At the same time, the crater walls become more and more gentle. This effect can be associated with an increase in the diffusion coefficient of atoms migrating against the concentration gradient.

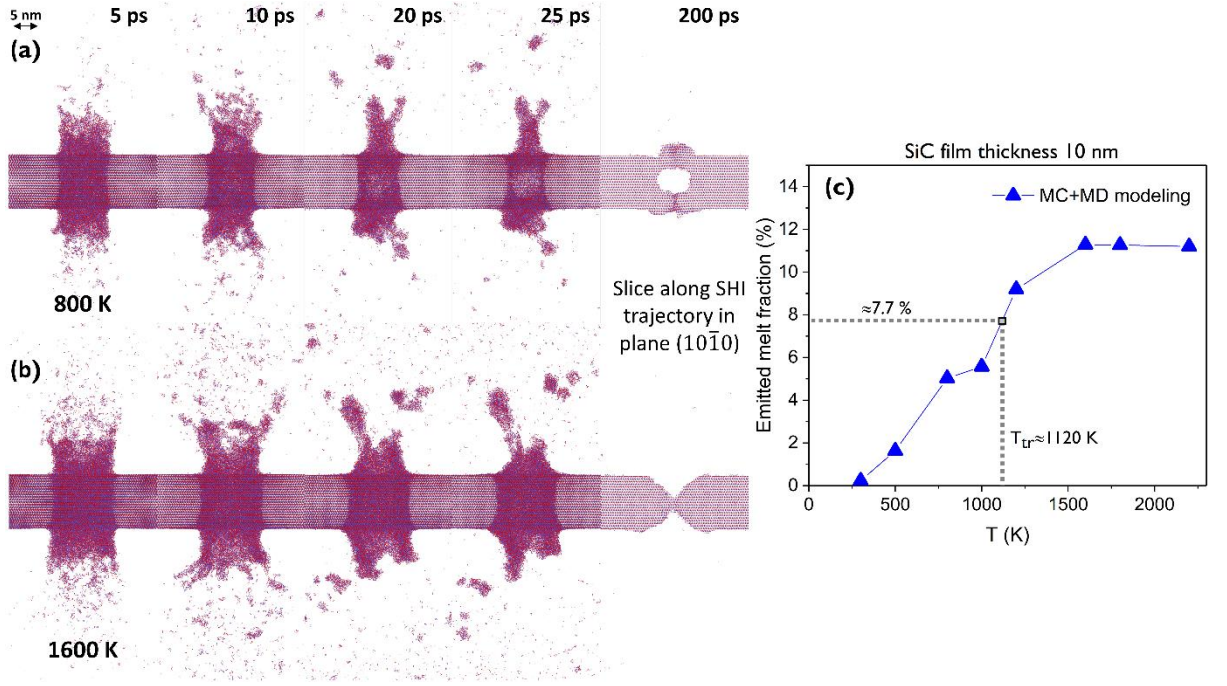


Fig. 9 Evolution of a 10 nm-thick SiC film after impact of a 710 MeV Bi ion (a) at 800 K and (b) at 1600 K; (c) fraction of ejected melt from a 10 nm-thick film consisting of 797040 atoms as a function of irradiation temperature.

Fig. 8b illustrate the threshold temperature at which hillocks transform into craters changing the morphology of the irradiated surface (see Fig. 8a). For a 10 nm thick film, the transition temperature is $T_{tr} \approx 1120$ K (see Fig. 8b). This transition can be associated with the enhancing effect of irradiation temperature on lattice heating from excited electrons in the track. As a result, the process of melt displacement to the film surface in the track region, which dominates at temperatures $T_{irr} < T_{tr}$ (see Fig. 9a) and leads to the formation of hillocks, is replaced by the process of ejection of matter droplets at $T_{irr} > T_{tr}$ (see Fig. 9b), which leads to the craters formation. The crater formation requires ejecting more than $\sim 7.7\%$ of the melt from the track (see Fig. 9c). This fraction may vary depending on the film thickness. The experimental observation of a similar transition under irradiation of LiF crystal with Xe ion is presented in Ref. [42] where an increase in local heating in the track was achieved by increasing the charge of the Xe ion from +15 to +36 (in units of electron charge).

It is also worth mentioning the experiment on oblique irradiation of SiC with 117 MeV Pb ions [43], where the formation of nanochannels with a depth of ≈ 0.2 nm was observed. The appearance of the temperature in the channel required for the ejection of the critical fraction of melt from the track in this experiment was achieved according to the mechanism described in Ref. [44]. This mechanism explains the enhanced heating of the near-surface layer of the film under oblique irradiation due to the reflection of excited electrons and valence holes from the surface.

3.3. Structural changes in SiC films of different thicknesses

In this section, we considered Bi 710 MeV ion irradiation of SiC films with thicknesses ranging from 10 nm to 100 nm across a wide temperature range.

At room irradiation temperature, the track region undergoes the following stages of evolution regardless of the film thickness: (i) formation of a molten cylindrical region, (ii) “squeezing” a part of the melt onto the film surface, and (iii) recrystallization of the molten region. As a result, hillocks were formed on the film surface and nanocavities remained in the film volume along the ion trajectory. However, the shape, size, and crystallinity of the hillocks, as well as the distribution of nanocavities and defect clusters in the film volume change with the film thickness.

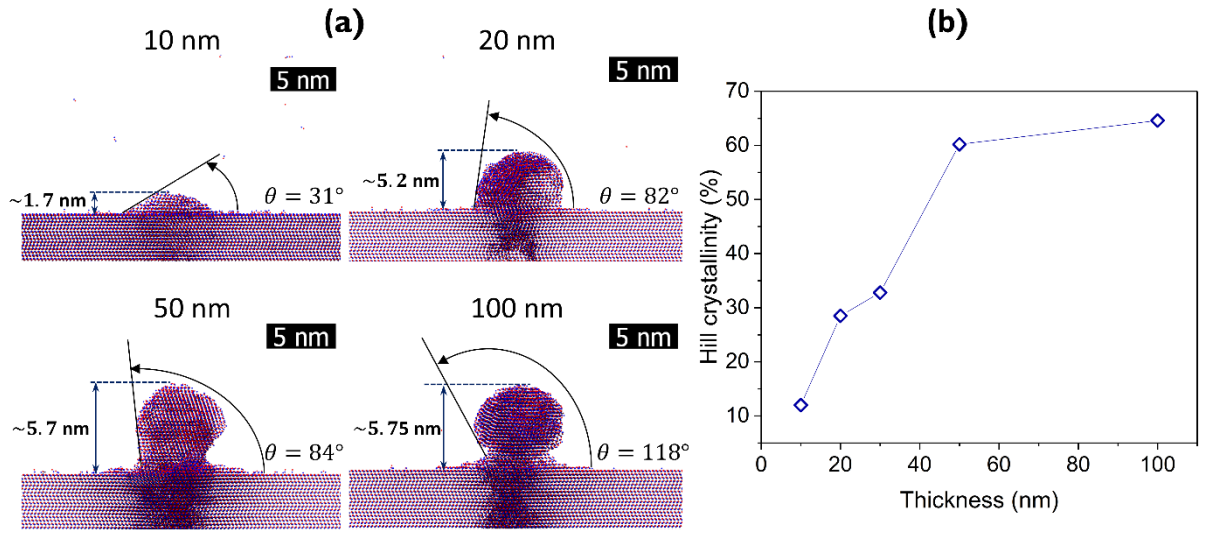


Fig. 10 (a) Hillocks on the surface of SiC film with thicknesses of 10 nm, 20 nm, 50 nm, and 100 nm after impact of a 710 MeV Bi ion at 300 K, (b) Dependence of hillock crystallinity on the thickness of SiC film irradiated with Bi 710 MeV ion at 300 K.

Fig. 10a shows that increasing the thickness of the irradiated film from 10 nm to 100 nm leads to an increase in the height of the hillocks on its surface from 1.7 nm to 5.75 nm, as well as an increase in the value of the contact angle from 31° to 118° . The fraction of the crystalline state identical to that in the original crystal also increases with film thickness from 12% for a 10 nm film to 65% for 100 nm film (see Fig. 10b). Thus, we show that the shape of the hillock and its crystallinity is determined not only by the balance of adhesion and cohesive forces within the melt, as reported in Ref. [45], but also by the amount of molten material that is “squeezed” onto the film surface from the track region. As a result, hillocks of predominantly crystalline composition with a shape close to spherical and a height of about 5.7 nm will be formed on the surface of bulk films after irradiation with 710 MeV Bi ion at room temperature.

The hillock formation on the surface of the films at $T_{irr} = 300$ K is accompanied by structural changes in the deeper regions. In films up to 100 nm thick, a chain of nanocavities surrounded by clusters of defects is formed along the ion trajectory (see Fig. 11). While in 10 nm thick film dislocations are formed in the bulk of the film along the edges of the defect region (see Fig. 7a). In thicker films dislocations were formed only in the 10 nm layer near the surface.

Fig. 11 shows that in a 100 nm thick film the track can be clearly divided into a near-surface region and a bulk region. In the near-surface region, this track consists of nanocavities and defect clusters and has a conical shape with a base diameter of $d \approx 4.4$ nm and a height of $H \approx 35$ nm. In the bulk region, several point defects remain along the ion trajectory, which is in agreement with previous calculations [9,37,46,47] and experimental data [48,49]. The track morphology in such a film at $T_{irr} = 300$ K is very similar to the experimental data on tracks at the boundary between Ti and SiC in Schottky diodes irradiated at 200 V by Ta¹⁸¹ ions with energy 1437.6 MeV [50]. We also observe a qualitative similarity with the experimental data from [51], in which the excitation of the atomic subsystem of SiC was induced by laser irradiation. However, in [51] due to the specificity of laser irradiation, in contrast to the SHI track, nanohillocks are formed around the excited region. Increasing the irradiation temperature in a 100 nm thick film leads to an increase in the size of the defect region with nanocavities and defect clusters deep into the film. Already at 1200 K, this region occupies the entire volume of the film along the ion trajectory.

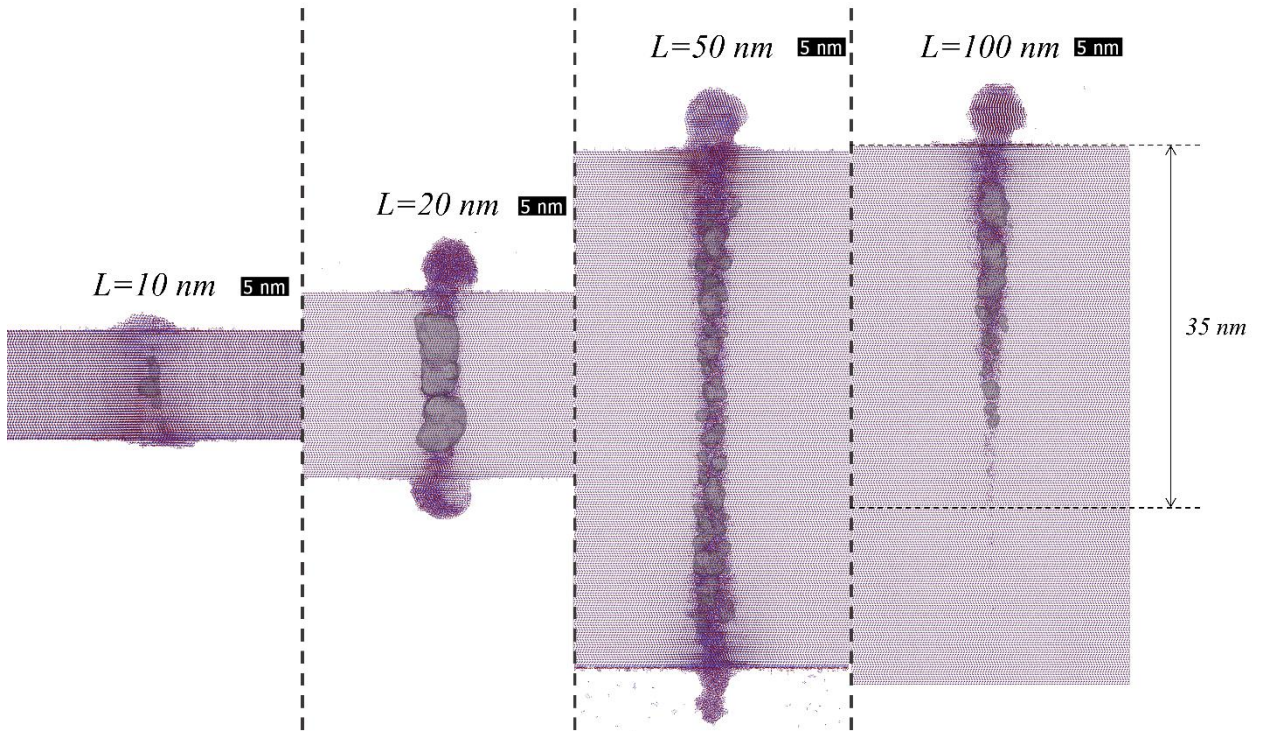


Fig. 11 Structure changes in SiC films of 10 nm, 20 nm, 50 nm, 100 nm thicknesses with highlighted surfaces of nanocavities after irradiation with 710 MeV Bi ion at room temperature.

We also found a transition from hillocks to craters with increasing irradiation temperature for films of different thicknesses. The film thickness increase led to a change from droplet ejection at high irradiation temperatures, which we observed in the 10 nm thick film (see Fig. 9b), to jet ejection, such as shown in Fig. 12 for 100 nm thick film - the thickest of the films we considered.

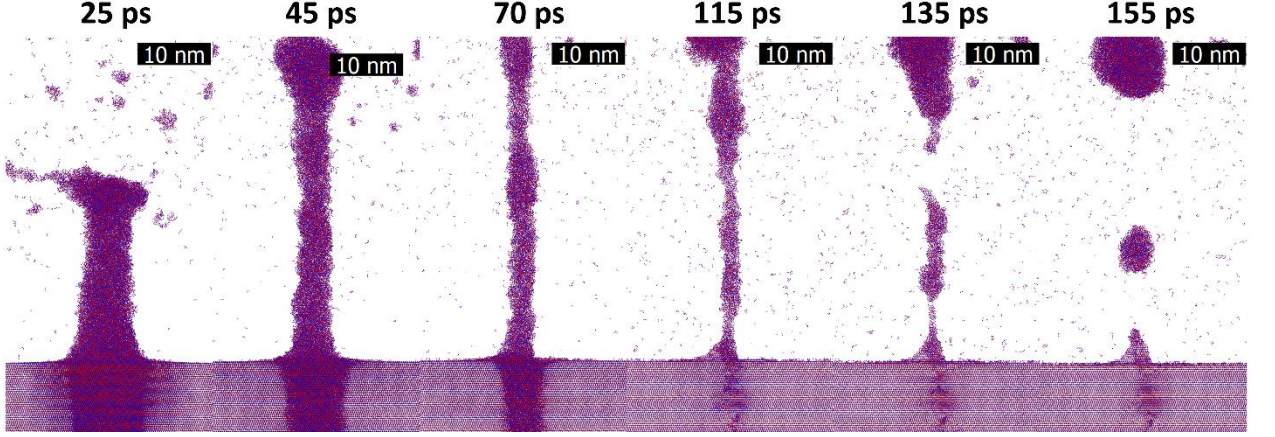


Fig. 12 Temporal evolution of the near-surface region of a 100 nm thick SiC film after an impact of a 710 MeV Bi ion at 1200 K.

Fig. 13a shows the dependence of hillock height and crater depth on the irradiation temperature for films of different thicknesses. From these curves we determined the transition temperatures from hillocks to craters, which are shown in Fig. 13b for different film thicknesses. It can be seen that the transition temperature increases with the film thickness.

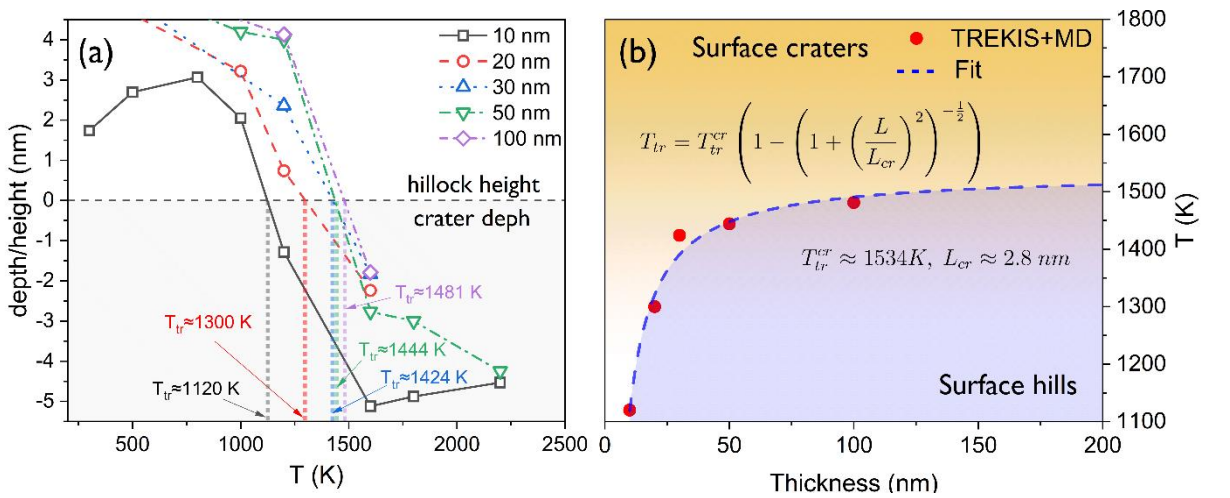


Fig. 13 (a) Average hillock height (positive) and crater depth (negative) of nanostructures created on the SiC (001) surface after Bi 710 MeV impact at different irradiation temperatures; (b) Transition temperature as a function of film thickness.

Apparently, this trend is associated with the threshold amount of substance that must be “ejected” from the film volume in the track region to form craters on its surface. The thicker the film, the more material needs to be ejected from it, and the stronger the heating of the track region required. Thus, the transition temperature should increase with increasing film thickness and reach a constant value for macroscopic samples, where it will be necessary to eject matter only from the subsurface region. In our simulations we observe a plateau already at thicknesses ≥ 30 nm. Our data are best described by a function of the form:

$$T_{tr} = T_{tr}^{cr} \left(1 - \left(1 + \left(\frac{L}{L_{cr}} \right)^2 \right)^{-\frac{1}{2}} \right) \quad (9)$$

Here $T_{tr}^{cr} \approx 1534$ K, $L_{cr} \approx 2.8$ nm (see Fig. 13b).

Extrapolation of this expression to the region of films of macroscopic thickness predicts a transition temperature from hillocks to craters of ≈ 1534 K. Thus, function (9) (see Fig. 13b) allowed us to divide the temperature-thickness scale for all films into two regions: (i) the region with hillock formation and (ii) the region with crater formation. However, this separation is approximate, because in films thicker than 30 nm we found the formation of combined structures near the transition temperature: formation of a hill in the center of the crater on one side of the film, as shown in Fig. 14, and a crater on the other side.

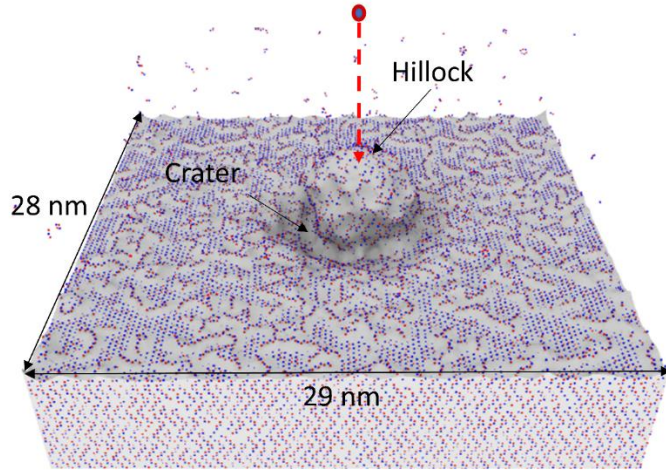


Fig. 14 Hillock formation inside a crater in a 100 nm thick SiC film after an impact of a 710 MeV Bi ion at 1600 K.

4. Conclusions

The results obtained in this work clarify the role of the surface in the formation and final structure of SHI tracks in SiC films.

In particular, we found that electron emission has a significant influence on the profile of the energy transferred to the atomic lattice in the SHI track only at very high irradiation temperatures ≥ 2200 K. In calculations that take into account emission, less energy is transferred to the lattice in the track than in calculations that do not take it into account. We also found that the enhancement of lattice heating in the central region of SHI track with increasing irradiation temperature established with periodic boundaries in [9] is preserved in thin films with open surfaces.

By modeling the irradiation of the films with a 710 MeV Bi ion at room temperature, we found that increasing the film thickness leads to an increase in the height of the hillocks on its surface from 1.7 nm for 10 nm films to 5.7 nm for ≥ 50 nm films. This increase is accompanied by an increase in the hillock sphericity and crystallinity.

At high irradiation temperatures, we observed a transition from hillocks to craters after Bi 710 MeV irradiation. For films of varying thicknesses ranging from 10 nm to 100 nm, we investigated the relationship between the irradiation temperature at which hillocks on the film surface transform into craters and the film thickness. We found the dependence of the transition temperature governing this transformation on the film thickness. This temperature increases with the film thickness from ≈ 1120 K for a 10 nm thick film to ≈ 1481 K for a 100 nm film. Extrapolating this dependence to the bulk film region predicts a transition temperature of ≈ 1534 K.

The work was carried out for the further development of high-tech processing of track detectors as a basic component in solving new problems of experimental nuclear physics. In particular, the paper shows a possible damage mechanism of Schottky barrier SiC detectors [52] and SiC-based miniature devices exposed to irradiation by SHIs under extreme conditions. Our findings can be used to extend the lifetime of these technologies. Moreover, these results can be used for controlled SiC surface texturing. For example, the creation of craters can be used to increase the light absorption required for energy conversion devices.

Code and data availability

The TREKIS-3 [14,15] code, used to model the excitation of the electronic and ionic systems in the SHI track, is available from [53]. The LAMMPS code was used for molecular dynamic calculations [54]. Ovito [55] software was used for visualization of MD calculations.

Acknowledgements

This work has been carried out using computing resources of the federal collective usage center Complex for Simulation and Data Processing for Mega-science Facilities at NRC “Kurchatov Institute”, <http://ckp.nrcki.ru/>. We are grateful to S.A. Gorbunov for helpful discussions and comments on the paper.

Author contributions: CRediT

D.I. Zainutdinov: Conceptualization; Formal Analysis; Methodology; Visualization; Writing – original draft; Writing – review & editing. **A.E. Volkov:** Conceptualization; Formal Analysis; Methodology; Project administration; Writing – review & editing.

References

- [1] A.E. Kaloyeros, B. Arkles, Silicon Carbide Thin Film Technologies: Recent Advances in Processing, Properties, and Applications - Part I Thermal and Plasma CVD, ECS J. Solid State Sci. Technol. 12 (2023) 103001. <https://doi.org/10.1149/2162-8777/acf8f5>.
- [2] F.H. Ruddy, L. Ottaviani, A. Lyoussi, C. Destouches, O. Palais, C. Reynard-Carette, Silicon Carbide Neutron Detectors for Harsh Nuclear Environments: A Review of the State of the Art, IEEE Trans. Nucl. Sci. 69 (2022) 792–803. <https://doi.org/10.1109/TNS.2022.3144125>.
- [3] X. Zhang, Y. Cao, C. Chen, L. Wu, Z. Wang, S. Su, W. Zhang, L. Lv, X. Zheng, W. Tian, X. Ma, Y. Hao, Study on Single Event Effects of Enhanced GaN HEMT Devices under Various Conditions, Micromachines 15 (2024). <https://doi.org/10.3390/mi15080950>.
- [4] A.F. Witulski, D.R. Ball, K.F. Galloway, A. Javanainen, J.-M. Lauenstein, A.L. Sternberg, R.D. Schrimpf, Single-Event Burnout Mechanisms in SiC Power MOSFETs, IEEE Trans. Nucl. Sci. 65 (2018) 1951–1955. <https://doi.org/10.1109/TNS.2018.2849405>.
- [5] C. Liu, G. Guo, H. Shi, Z. Zhang, F. Li, Y. Zhang, J. Han, Study on the Single-Event Burnout Effect Mechanism of SiC MOSFETs Induced by Heavy Ions, Electronics 13 (2024) 3402. <https://doi.org/10.3390/electronics13173402>.
- [6] Y. Katoh, L.L. Snead, Silicon carbide and its composites for nuclear applications – Historical overview, J. Nucl. Mater. 526 (2019) 151849. <https://doi.org/10.1016/j.jnucmat.2019.151849>.
- [7] A. Debelle, L. Thomé, I. Monnet, F. Garrido, O.H. Pakarinen, W.J. Weber, Ionization-induced thermally activated defect-annealing process in SiC, Phys. Rev. Mater. 3 (2019) 1–11. <https://doi.org/10.1103/PhysRevMaterials.3.063609>.
- [8] E. Kucal, P. Jóźwik, C. Mieszczyński, R. Heller, S. Akhmadaliev, C. Dufour, K. Czerski, Temperature Effects of Nuclear and Electronic Stopping Power on Si and C Radiation Damage in 3C-SiC, Materials (Basel). 17 (2024) 2843.

<https://doi.org/10.3390/ma17122843>.

- [9] D.I. Zainutdinov, V.A. Borodin, S.A. Gorbunov, N. Medvedev, R.A. Rymzhanov, M.V. Sorokin, R.A. Voronkov, A.E. Volkov, High-temperature threshold of damage of SiC by swift heavy ions, *J. Alloys Compd.* 1013 (2024) 1–29. <https://doi.org/10.1016/j.jallcom.2025.178524>.
- [10] D.I. Zainutdinov, R.A. Voronkov, S.A. Gorbunov, N. Medvedev, R.A. Rymzhanov, M. V. Sorokin, A.E. Volkov, Modeling of Temperature Effects on the Formation of Tracks of Swift Heavy Ions in Silicon Carbide, *J. Surf. Investig. X-Ray, Synchrotron Neutron Tech.* 2024 183 18 (2024) 683–689. <https://doi.org/10.1134/S1027451024700319>.
- [11] R.A. Rymzhanov, N. Medvedev, A.E. Volkov, Damage kinetics induced by swift heavy ion impacts onto films of different thicknesses, *Appl. Surf. Sci.* 566 (2021) 150640. <https://doi.org/10.1016/j.apsusc.2021.150640>.
- [12] R.A. Rymzhanov, A.E. Volkov, V.A. Skuratov, Bulk, overlap and surface effects of swift heavy ions in CeO₂, *J. Nucl. Mater.* 604 (2025) 155480.
- [13] N. Ishikawa, N. Okubo, T. Taguchi, Experimental evidence of crystalline hillocks created by irradiation of CeO₂ with swift heavy ions: TEM study, *Nanotechnology* 26 (2015) 355701. <https://doi.org/10.1088/0957-4484/26/35/355701>.
- [14] N.A. Medvedev, R.A. Rymzhanov, A.E. Volkov, Time-resolved electron kinetics in swift heavy ion irradiated solids, *J. Phys. D. Appl. Phys.* 48 (2015) 355303. <https://doi.org/10.1088/0022-3727/48/35/355303>.
- [15] R.A. Rymzhanov, N.A. Medvedev, A.E. Volkov, Effects of model approximations for electron, hole, and photon transport in swift heavy ion tracks, *Nucl. Instruments Methods Phys. Res. Sect. B Beam Interact. with Mater. Atoms* 388 (2016) 41–52. <https://doi.org/10.1016/j.nimb.2016.11.002>.
- [16] R.A. Rymzhanov, N.A. Medvedev, A.E. Volkov, Electron emission from silicon and germanium after swift heavy ion impact, *Phys. Status Solidi B* 252 (2015) 159–164. <https://doi.org/10.1002/pssb.201400130>.
- [17] S. Plimpton, Fast Parallel Algorithms for Short-Range Molecular Dynamics, *J. Comput. Phys.* 117 (1995) 1–19. <https://doi.org/10.1006/jcph.1995.1039>.
- [18] Z. Liu, X. Cheng, X. Yang, M. Liu, R. Liu, B. Liu, Y. Tang, Ultra-high temperature microstructural changes of SiC layers in TRISO particles, *Ceram. Int.* 50 (2024) 2331–2339. <https://doi.org/https://doi.org/10.1016/j.ceramint.2023.11.007>.
- [19] N. Medvedev, A.E. Volkov, R. Rymzhanov, F. Akhmetov, S. Gorbunov, R. Voronkov, P. Babaev, Frontiers, challenges, and solutions in modeling of swift heavy ion effects in materials, *J. Appl. Phys.* 133 (2023) 100701. <https://doi.org/10.1063/5.0128774>.
- [20] N.A. Medvedev, A.E. Volkov, Nonthermal acceleration of atoms as a mechanism of fast lattice heating in ion tracks, *J. Appl. Phys.* 225903 (2022) 131. <https://doi.org/10.1063/5.0095724>.
- [21] L. Van Hove, Correlations in Space and Time and Born Approximation Scattering in Systems of Interacting Particles, *Phys. Rev.* 95 (1954) 249–262. <https://doi.org/10.1103/PhysRev.95.249>.
- [22] L. Johansson, F. Owman, P. Mårtensson, C. Persson, U. Lindefelt, Electronic structure of 6H-SiC(0001), *Phys. Rev. B - Condens. Matter Mater. Phys.* 53 (1996) 13803–13807. <https://doi.org/10.1103/PhysRevB.53.13803>.
- [23] A. Chvála, R. Szobolovszký, J. Kovác, M. Florovic, J. Marek, L. Cernaj, D. Donoval, C.

- Dua, S.L. Delage, J.C. Jacquet, Advanced characterization techniques and analysis of thermal properties of AlGaIn/GaN Multifinger Power HEMTs on SiC substrate supported by three-dimensional simulation, *J. Electron. Packag. Trans. ASME* 141 (2019). <https://doi.org/10.1115/1.4043477>.
- [24] M. Bauer, A.M. Gigler, A.J. Huber, R. Hillenbrand, R.W. Stark, Temperature-depending Raman line-shift of silicon carbide, *J. Raman Spectrosc.* 40 (2009) 1867–1874. <https://doi.org/10.1002/jrs.2334>.
 - [25] P.H. Berens, D.H.J. Mackay, G.M. White, K.R. Wilson, Thermodynamics and quantum corrections from molecular dynamics for liquid water, *J. Chem. Phys.* 79 (1983) 2375–2389. <https://doi.org/10.1063/1.446044>.
 - [26] J.S. Bader, B.J. Berne, Quantum and classical relaxation rates from classical simulations, *J. Chem. Phys.* 100 (1994) 8359–8366. <https://doi.org/10.1063/1.466780>.
 - [27] L. Frommhold, COLLISION-INDUCED ABSORPTION IN GASES, 1993.
 - [28] C. Kittel, C.Y. (Ching-yao) Fong, Quantum theory of solids, Wiley, 1987.
 - [29] W.H. Barkas, Nuclear research emulsions., Academic Press, New York, 1963. <http://hdl.handle.net/2027/uc1.b3533401> (accessed November 20, 2013).
 - [30] C. Bouchard, J.D. Carette, The Surface Potential Barrier in Secondary Emission from Semiconductors, *Surf. Sci.* 100 (1980) 251–268.
 - [31] C. Eckart, The penetration of a potential barrier by electrons, *Phys. Rev.* 35 (1930) 1303–1309. <https://doi.org/10.1103/PhysRev.35.1303>.
 - [32] J. Cazaux, Calculated dependence of few-layer graphene on secondary electron emissions from SiC, *Appl. Phys. Lett.* 98 (2011). <https://doi.org/10.1063/1.3534805>.
 - [33] V.S. Fomenko, Handbook of Emission Properties of Materials, Kiev Nauk. Dumka (1981) 6.
 - [34] P. Vashishta, R.K. Kalia, A. Nakano, J.P. Rino, Interaction potential for silicon carbide: A molecular dynamics study of elastic constants and vibrational density of states for crystalline and amorphous silicon carbide, *J. Appl. Phys.* 101 (2007). <https://doi.org/10.1063/1.2724570>.
 - [35] J.S. Alexander, C. Maxwell, J. Pencer, M. Saoudi, Equilibrium Molecular Dynamics Calculations of Thermal Conductivity: a “How-To” for the Beginners, *CNL Nucl. Rev.* 9 (2020) 11–25. <https://doi.org/10.12943/cnr.2018.00009>.
 - [36] R. Rymzhanov, N.A. Medvedev, A.E. Volkov, Damage threshold and structure of swift heavy ion tracks in Al₂O₃, *J. Phys. D. Appl. Phys.* 50 (2017) 475301. <https://doi.org/10.1088/1361-6463/aa8ff5>.
 - [37] M. Backman, M. Toulemonde, O.H. Pakarinen, N. Juslin, F. Djurabekova, K. Nordlund, A. Debelle, W.J. Weber, Molecular dynamics simulations of swift heavy ion induced defect recovery in SiC, *Comput. Mater. Sci.* 67 (2013) 261–265. <https://doi.org/https://doi.org/10.1016/j.commatsci.2012.09.010>.
 - [38] H.J.C. Berendsen, J.P.M. Postma, W.F. van Gunsteren, A. DiNola, J.R. Haak, Molecular dynamics with coupling to an external bath, *J. Chem. Phys.* 81 (1984) 3684–3690. <https://doi.org/10.1063/1.448118>.
 - [39] R.A. Rymzhanov, N. Medvedev, A.E. Volkov, Damage kinetics induced by swift heavy ion impacts onto films of different thicknesses, *Appl. Surf. Sci.* 566 (2021) 150640. <https://doi.org/10.1016/J.APSUSC.2021.150640>.

- [40] L. Zeng, X. Zhou, R. Cheng, X. Wang, J. Ren, Y. Lei, L. Ma, Y. Zhao, X. Zhang, Z. Xu, Temperature and energy effects on secondary electron emission from SiC ceramics induced by Xe¹⁷⁺ ions, *Sci. Rep.* 7 (2017) 1–6. <https://doi.org/10.1038/s41598-017-06891-9>.
- [41] E.J. Sternglass, Theory of secondary electron emission by high-speed ions, *Phys. Rev.* 108 (1957) 1–12. <https://doi.org/10.1103/PhysRev.108.1>.
- [42] A.S. El-Said, R.A. Wilhelm, R. Heller, M. Sorokin, S. Facsko, F. Aumayr, Tuning the Fabrication of Nanostructures by Low-Energy Highly Charged Ions, *Phys. Rev. Lett.* 117 (2016) 1–5. <https://doi.org/10.1103/PhysRevLett.117.126101>.
- [43] O. Ochedowski, O. Osmani, M. Schade, B.K. Bussmann, B. Ban-d’Etat, H. Lebius, M. Schleberger, B. Ban-Detat, H. Lebius, M. Schleberger, Graphitic nanostripes in silicon carbide surfaces created by swift heavy ion irradiation, *Nat. Commun.* 5 (2014) 3913. <https://doi.org/10.1038/ncomms4913>.
- [44] R.A. Rymzhanov, M. Ćosić, N. Medvedev, A.E. Volkov, From groove to hillocks – Atomic-scale simulations of swift heavy ion grazing impacts on CaF₂, *Appl. Surf. Sci.* 652 (2024). <https://doi.org/10.1016/j.apsusc.2024.159310>.
- [45] N. Ishikawa, T. Taguchi, H. Ogawa, Comprehensive Understanding of Hillocks and Ion Tracks in Ceramics Irradiated with Swift Heavy Ions, *Quantum Beam Sci.* 2020, Vol. 4, Page 43 4 (2020) 43. <https://doi.org/10.3390/QUBS4040043>.
- [46] Y. Zhang, R. Sachan, O.H. Pakarinen, M.F. Chisholm, P. Liu, H. Xue, W.J. Weber, Ionization-induced annealing of pre-existing defects in silicon carbide, *Nat. Commun.* 6 (2015) 1–7. <https://doi.org/10.1038/ncomms9049>.
- [47] A. Debelle, M. Backman, L. Thomé, W.J. Weber, M. Toulemonde, S. Mylonas, A. Boulle, O.H. Pakarinen, N. Juslin, F. Djurabekova, K. Nordlund, F. Garrido, D. Chaussende, Combined experimental and computational study of the recrystallization process induced by electronic interactions of swift heavy ions with silicon carbide crystals, *Phys. Rev. B* 86 (2012) 100102. <https://doi.org/10.1103/PhysRevB.86.100102>.
- [48] S. Nan, M. Xiao, Z. Guan, C. Feng, C. Huo, G. Li, P. Zhai, F. Zhang, Atomic-scale revealing defects in ion irradiated 4H-SiC, *Mater. Charact.* 203 (2023) 113125. <https://doi.org/10.1016/j.matchar.2023.113125>.
- [49] S.J. Zinkle, J.W. Jones, V.A. Skuratov, Microstructure of swift heavy ion irradiated SiC, Si₃N₄ and AlN, *Mater. Res. Soc. Symp. - Proc.* 650 (2001) 1–6. <https://doi.org/10.1557/proc-650-r3.19>.
- [50] X. Yan, P. Zhai, C. Yang, S. Zhao, S. Nan, P. Hu, T. Zhang, Q. Chen, L. Xu, Z. Li, J. Liu, Unveiling microstructural damage for leakage current degradation in SiC Schottky diode after heavy ions irradiation under 200 V, *Appl. Phys. Lett.* 125 (2024). <https://doi.org/10.1063/5.0216883>.
- [51] A. Medvid, B. Berzina, L. Trinkler, L. Fedorenko, P. Lytvyn, N. Yusupov, T. Yamaguchi, L. Sirghi, M. Aoyama, Formation of nanostructure on surface of SiC by laser radiation, *Phys. Status Solidi Appl. Res.* 195 (2003) 199–203. <https://doi.org/10.1002/pssa.200306281>.
- [52] M. De Napoli, SiC detectors: A review on the use of silicon carbide as radiation detection material, *Front. Phys.* 10 (2022) 1–28. <https://doi.org/10.3389/fphy.2022.898833>.
- [53] N. Medvedev, R. Rymzhanov, A. Volkov, TREKIS-3 [Computer Software], (2023) <https://doi.org/10.5281/zenodo.8394462>. <https://doi.org/10.5281/zenodo.8394462>.
- [54] S. Plimpton, Fast Parallel Algorithms for Short-Range Molecular Dynamics, *J Comp Phys* 117 (1995) 1–19.

- [55] A. Stukowski, Visualization and analysis of atomistic simulation data with OVITO—the Open Visualization Tool, *Model. Simul. Mater. Sci. Eng.* 18 (2010) 15012. <https://doi.org/10.1088/0965-0393/18/1/015012>.